Materials Research Proceedings **27** (2023) 50-58 https://doi.org/10.21741/9781644902455-7

The effect of positional instability on the detection of barely visible impact damage in composites using a mobile thermographic inspection robot

Jaslyn Gray[1,a *], Mark Richards[1,b], Peter Muir[1,c], Hamish Self[1,d], Cedric Rosalie[1,e] and Nik Rajic[1,f]

[1] Defence Science and Technology Group, 506 Lorimer Street, Fishermans Bend, VIC, 3207, Australia

[a]jaslyn.gray@defence.gov.au, [b]mark.richards19@defence.gov.au, [c]peter.muir7@defence.gov.au, [d]hamish.self@defence.gov.au, [e]cedric.rosalie1@defence.gov.au, [f]nikolas.rajic@defence.gov.au

Keywords: Line Scan Thermography, Composite Materials, Positional Instability, Non-Destructive Inspection, Robotic Inspection, Infrared Imaging

Abstract. As the use of composite materials continues to expand within the aerospace domain and elsewhere, the demand for rapid impact damage detection capabilities is also increasing. Line-scan thermography (LST) is a promising inspection modality where a light source focused to a line is swept over a structural component and sub-surface damage is highlighted as a thermal signature detectable via infrared imaging. This paper presents a rapid LST robotic inspection system combining ground-based robotics, advanced infrared imaging technology and dynamic image processing that is capable of achieving detection of barely visible impact damage in composite structures. The robotic system is evaluated experimentally on carbon fibre composite laminate specimens containing synthetic flat-bottom-hole defects, at scan speeds ranging from 25 mm/s to 100 mm/s. A study into the effect of positional instability on the capacity of the inspection system to detect damage is undertaken by introducing controlled perturbations in the robot path. Finite element modelling is also presented and verified against experimental results. Understanding the effect of positional instability on defect detection is important as work progresses towards an aerial drone-based implementation of this inspection capability.

Introduction

The use of carbon-fibre-reinforced polymer (CFRP) composite components in aircraft construction continues to grow, driven by significant performance and sustainment-related advantages relative to metals, which include higher strength and stiffness-to-weight ratio and increased resistance to corrosion and fatigue [1]. One comparative disadvantage of CFRP is its increased vulnerability to impact from events such as accidental tool drop, runway debris and bird strike, which can result in barely visible impact damage (BVID). BVID, by definition, is difficult to detect via visual inspection yet the degradation caused by low-velocity impact can lead to significant strength reduction, and if not managed, eventual component failure [2, 3]. Development of improved methods of BVID detection and quantification is of significant interest to aircraft operators, especially rapidly deployable methods that minimise aircraft down-time. This need has driven investigation of using remotely driven ground and aerial robotic platforms for detecting and evaluating structural damage.

The use of uncrewed aerial vehicles (UAVs) for detection of visible structural damage in aircraft is well established. However, such capabilities are currently limited to visible surface defects and generally used as a tool to aid routine visual inspection performed by maintenance ground crew [4]. BVID detection is currently not achievable using such an approach. Instead, traditional non-destructive inspection (NDI) methods are used, such as liquid penetrant, ultrasonic testing, acoustic emission, eddy current testing and thermography [5], many of which are laborious and time consuming to implement.

Automation and robotic implementation of traditional NDI methods offers scope for improved inspection speed and coverage. However, adapting some of these to automation is not straightforward. Well-established NDI methods such as ultrasonic testing are relatively slow, especially when implemented manually, and because they typically require precise positioning and the use of an ultrasonic couplant, are not well suited to rapid wide-area inspection. Active thermography, a wide-area non-contact technique, provides a more encouraging basis for ground and aerial robotic deployment, as demonstrated in recent studies [6-17].

Several of these previous robotic implementations involve line-scan thermography (LST), e.g. [11-13, 15-17]. LST utilises a focused light source to generate a line of heat which is moved at constant speed over the test area. An infrared camera moving in unison with this heat source records the temperature response in the wake of the source [12]. The rate of heat dissipation is typically lower in regions of BVID, thus causing a corresponding ‘hot spot’, which can be highlighted using image processing methods.

A robotic implementation of LST to the inspection of BVID in polymer composite panels was reported previously in [17]. This implementation consisted of several key parts. The first is an infrared image processing method called dynamic pulse phase thermography (DPPT), detailed in [15], which simplifies the identification of defect signatures in LST data. As its name suggests, DPPT is a dynamic adaptation of pulse phase thermography (PPT) [18], whereby raw thermographic image frames from an LST inspection are processed via a fast Fourier transform (FFT) without the intermediate step of pseudo-static image reconstruction, which is typically required by other LST data processing algorithms [13]. In DPPT, BVID and other near-surface defects produce a characteristic dipole-shaped signature in the phase spectrum [15]. Another key element of this inspection capability is a high operating temperature (HOT) infrared detector, which previous work [16] has shown can match the performance of a conventional cooled photon-detector but with significantly reduced size, weight and power consumption, making it better suited to robotic applications [16].

The present paper reports on new work quantifying the performance of this robotic inspection capability, focusing on the effect of scan path instability on defect detectability using LST. Such instability is potentially a significant source of performance degradation for LST, especially for aerial drone implementation, which is the next step in the development of this capability.

Experimental Methodology

Thermographic Inspection Ground-based Evaluation Robot (TIGER)

The robotic platform used in the present work is called TIGER (Thermographic Inspection Ground-based Evaluation Robot), see Fig. 1. TIGER is approximately 295 x 355 x 140 mm in size, weighs ~20 kg, and is configured as a four-wheeled vehicle with two DC motors driving the front-right and back-left wheels, with the remaining two wheels allowed to spin freely. The robot is controlled by a Raspberry Pi 4b, which drives both motors, two ILR2250 Micro Epsilon laser distance sensors and a FLIR Neutrino LC HOT medium-wave infrared imager detailed previously in [14,15]. The luminaire consists of a 150 W quartz-halogen lamp and custom polished aluminium reflector designed to produce a line source with a beam width of approximately 20 mm (full-width at half maximum) at a focal length of 500 mm.

A typical BVID signature obtained from TIGER is shown in Fig. 2. In this example, the signature corresponds to a 10 J impact on a carbon-fibre laminate scanned at a velocity of 25 mm/s and has the characteristic dipole shape mentioned previously. While detection of BVID is the ultimate objective of TIGER, this particular study focuses on laminates containing only synthetic

Materials Research Proceedings **27** (2023) 50-58 https://doi.org/10.21741/9781644902455-7

flat-bottom-hole (FBH) defects, as these produce signatures with a consistency and predictability that is advantageous for the particular objectives of this study.

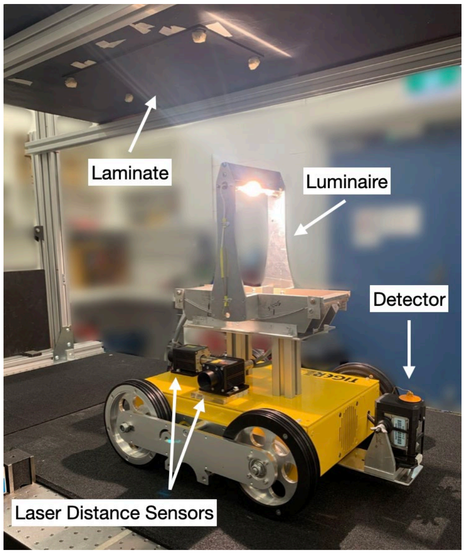

Fig. 1: TIGER platform for LST experimentation with luminaire, IR detector and laser distance sensors mounted.

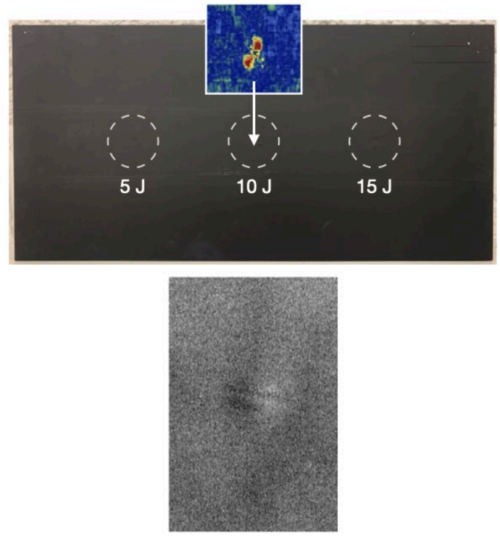

Fig. 2: At top is a photograph of test panel containing BVID with impact regions circled and an ultrasonic C-scan image of damage caused by a 10 J impact. At bottom is a corresponding DPPT signature.

FBH Test Specimens

Experimentation was undertaken on two carbon-fibre composite laminates each comprising 16 plies of M18/1/43% G939 carbon-epoxy biaxial material in a ($[0/\text{-}45/45/0]_4$) layup with a cured thickness of 3.8 mm. FBH defects of varying diameter and depth were machined into one side in the layout illustrated in Fig. 3. For the baseline scans (non-perturbed scan path) these laminates were inspected together in the end-to-end arrangement shown in Fig. 3, while for the perturbed scans only the panel containing the 10 mm and 5 mm FBH was used.

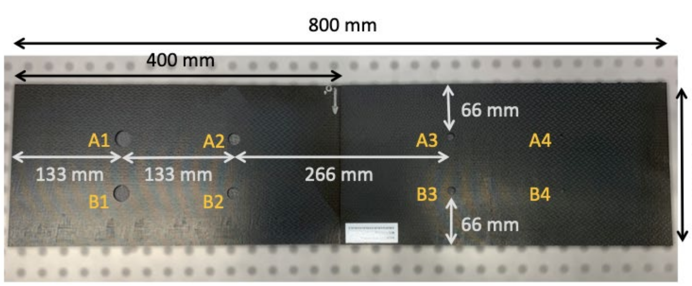

	Diameter (mm)	Depth (mm)		Diameter (mm)	Depth (mm)
A1	20	1	B1	20	1.5
A2	15	1	B2	15	1.5
A3	10	1	B3	10	1.5
A4	5	1	B4	5	1.5

Fig. 3: Underside of two composite panels each containing four FBH defects. Relevant FBH dimensions are listed on the right.

Scan Path Perturbation

In the present study, perturbations in TIGER's scan path were limited to a sinusoidal deviation perpendicular to the scan motion. This deviation was achieved by creating a difference in the left and right motor speeds, in accordance with the forward kinematics equations for a differential drive robot [19,20]. For a prescribed scan velocity and desired perturbation amplitude and period, the corresponding motor speeds can be determined from Eq. 1-4. The position of the robot during

Materials Research Proceedings **27** (2023) 50-58
https://doi.org/10.21741/9781644902455-7

each scan was tracked using measurements obtained from the aforementioned laser distance sensors, and then checked against a marked trace of TIGER's motion.

$$\delta(t) = \mathrm{A_p} \cdot \mathrm{sgn}(\sin(\omega t))\sin(2\omega t) \tag{1}$$

$$\omega = \frac{v_{scan}}{\lambda}\pi \tag{2}$$

$$v_{left}(t) = v_{scan} + \delta(t) \tag{3}$$

$$v_{right}(t) = v_{scan} - \delta(t) \tag{4}$$

Here, $\delta(t)$ is a time dependent sinusoidal perturbation in the linear scan speed, v_{scan}, which translates to corresponding speed curves for the left and right motors, $v_{left}(t)$ and $v_{right}(t)$ respectively. The amplitude of perturbation is represented by A_p, and the frequency of perturbation is represented by ω, which depends on v_{scan} and the wavelength of the perturbation, λ.

Three specific perturbation cases were examined, defined according to the detector path orientation at the moment a defect or set of defects appear mid-frame, as illustrated in Fig. 4. In this figure, the red trace represents the centroid of TIGER and the black trace the path of the detector mounted 300 mm behind the centroid. A wavelength of 790 mm was selected along with an amplitude of 10 mm, corresponding to twice the length of the test panel and the diameter of the largest considered FBH, respectively.

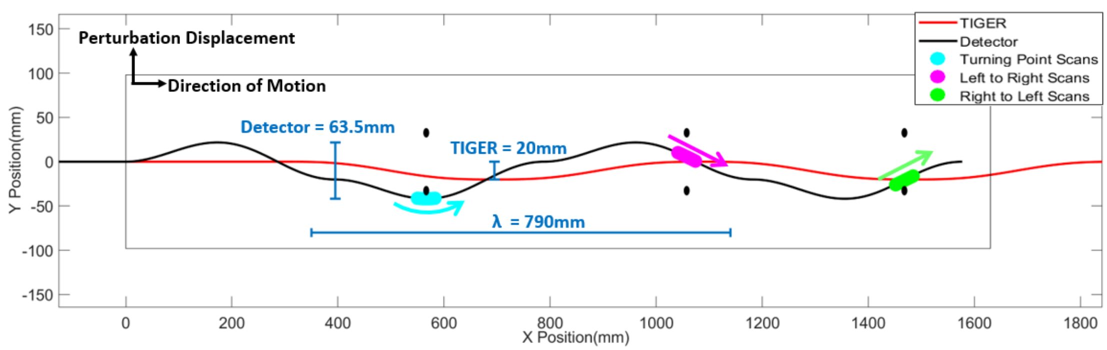

Fig. 4: Path traces for TIGER and detector at 25 mm/s. Arrows indicate detector direction over FBH defects for the targeted perturbation paths.

Results and Discussion

Scans were first undertaken without perturbing the scan path, to establish a baseline for the detection performance of TIGER. While scans were performed at a range of velocities, for the sake of brevity, only results corresponding to 25 mm/s and 100 mm/s are presented, as these represent practical velocity limits for the present implementation of TIGER. As shown in Fig. 5, all FBH defects, including the 5 mm diameter case, are detectible at a 25 mm/s scan speed. At 100 mm/s, the deepest defects produce weak but still discernible signatures for the 15 mm and 20 mm diameter cases, while shallower defects are detectible at diameters 10 mm and above.

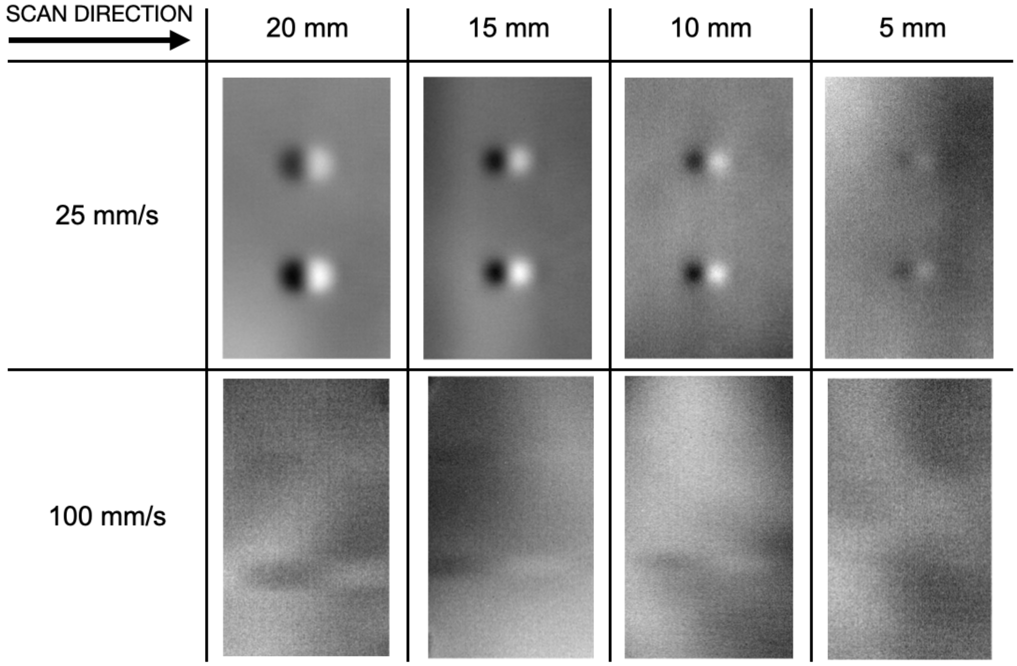

Fig. 5: DPPT dipole signatures for decreasing FBH diameters at 25 mm/s and 100 mm/s scan speeds, obtained using TIGER. Top and bottom signatures in each image correspond to FBH defects 1.5 mm and 1 mm below the surface, respectively (see Fig 3).

DPPT results for the three scan path orientations outlined in Fig. 4 are presented in Fig. 6 and Fig. 7 for the 10 mm and 5 mm diameter FBH defects, respectively, and correspond to a scan speed of 25 mm/s. Relative to the baseline signature, the effect of the considered perturbations on defect detectability is small enough to be considered insignificant. As expected, the perturbations produce a signature rotation and translation consistent with the scan orientation at the moment of defect traversal. Interestingly, the ‘Turning Point’ and ‘Left-to-Right' cases produce similar results, which is due to a similarity in the detector’s scan path over the processing time-window. A slight increase in background noise is observed in the DPPT perturbation results relative to the baseline scans, especially evident in the 5 mm case. This could potentially be due to the velocity of the heat source no longer being constant as it moves in an arc over the defects, or from vibrations induced in the system during turning of the robot, which caused noticeable wheel slippage.

While only modest changes in defect signature were observed in this study, the perturbations applied were of relatively small amplitude and large wavelength compared to the defect size. This constitutes a significant limitation in the present study as aerial implementations of this inspection capability are likely to also contain higher amplitude and broader wavelength perturbations. It is surmised that relatively high amplitude and short wavelength components should cause more significant signature degradation than observed here. Unfortunately, such components were not able to be studied due to limitations in the present experimental arrangement. A fixed Cartesian robot without these limitations has been developed and will be used to undertake a more comprehensive perturbation study, the results of which will be reported elsewhere.

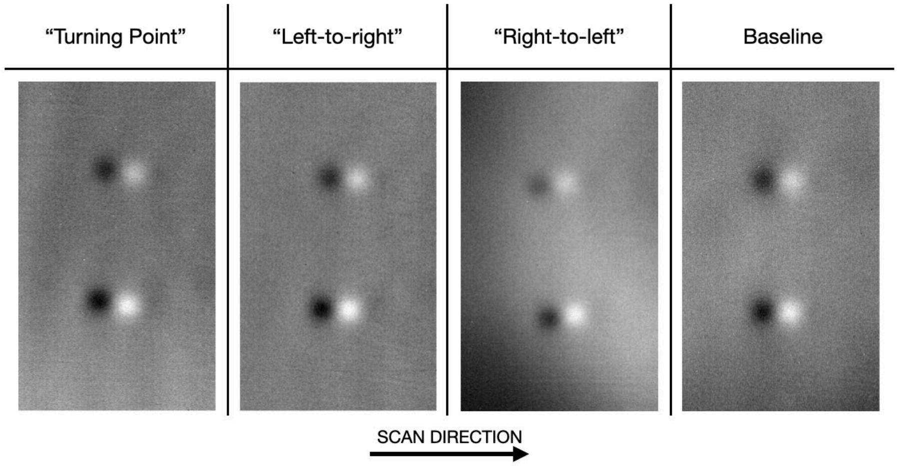

Fig. 6: DPPT dipole signatures for 10 mm diameter FBH defects for three perturbed scan path orientations (see Fig. 4) compared to baseline scan. Top and bottom signatures correspond to FBH defects located 1.5 mm and 1 mm below the surface respectively.

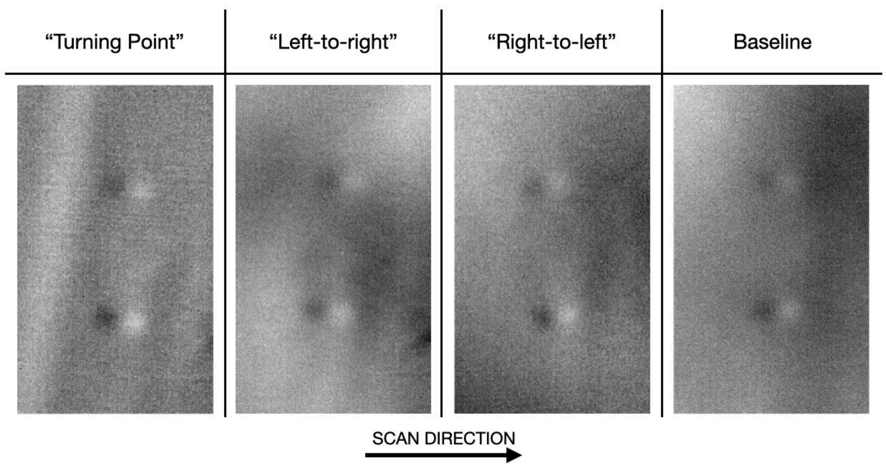

Fig. 7: As in Fig. 6 but for 5 mm diameter FBH defects.

It was remarked previously that synthetic FBH defects are advantageous for a perturbation study of this kind because of their consistency and predictability. Predictability is important from the viewpoint of being able to supplement experimental investigation of the effects of path instability with numerical investigation using predictive modelling, which has the advantage of being able to consider perturbation scenarios that would be difficult to reproduce experimentally. To this end, appropriate multi-physics simulations were undertaken to determine whether the perturbation effects visible in Fig. 6 and Fig. 7 could be reproduced in corresponding model predictions.

Using the COMSOL 5.5 software package, the FBH panel from Fig. 3 containing the 10 mm and 5 mm FBH was modelled with an additional material buffer of 50 mm in the *y* direction, to account for times where the detector field of view (FOV) travelled off the panel. Material properties used for this simulation can be found in previously reported work [16]. Fig. 8 (left) shows a surface temperature map of the modelled FBH panel corresponding to a time when the detector FOV was centred over the 10 mm defect. This surface data was then remapped in MATLAB to introduce a simulated "Right-to-left" path orientation (from Fig. 4) to match the experimental case. A comparison of the DPPT results for the modelled dipole to one obtained from TIGER is given to the right of Fig. 8. The TIGER result shows a translation of the lower dipole in the scan direction relative to the upper dipole. This offset is not reflected in the simulation since it did not account for the physical rotation of the camera and instead considered only the x and y axis translation in the given path. Notwithstanding, the predicted dipole signatures generally correlate well with the corresponding experimental results, providing confidence that modelling can in future be used to make predictions of the effect of path variation on the thermal signature of a defect.

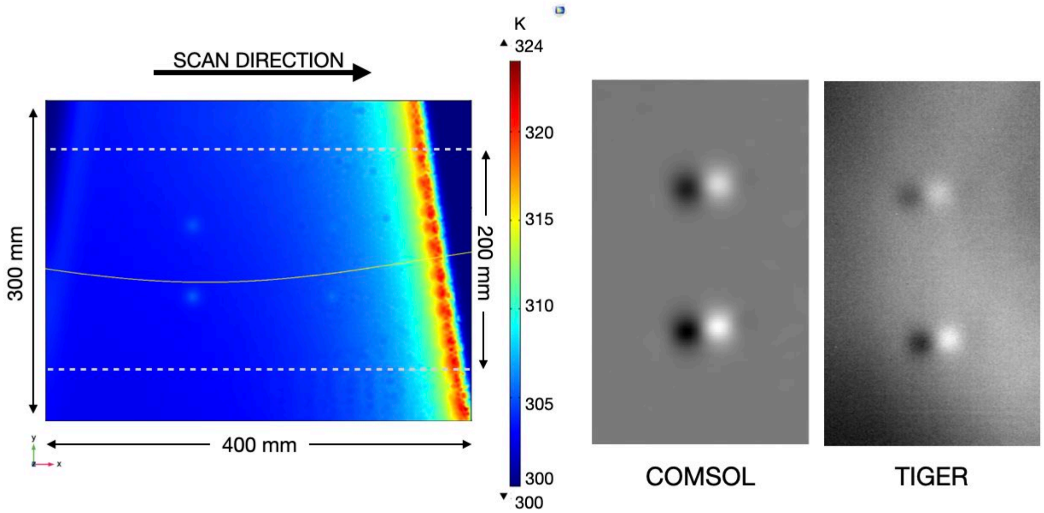

Fig. 8: (Left) Multi-physics model prediction of surface temperature distribution for a panel with 10 mm and 5 mm diameter FBH defects (from Fig. 1) scanned at 25 mm/s with a 20 mm peak-to-peak perturbation amplitude. Yellow line is a trace of TIGER's centroid. (Right) Comparison of FBH signatures for 10 mm diameter FBH from simulated and experimental scan results.

Conclusions

A ground-based robotic line-scan inspection platform has been evaluated on composite laminates containing synthetic flat-bottom-hole defects under perturbed scan path conditions to determine the effect of robot path instability on defect detectability. The study focused on FBH defects of varying diameter and depth inspected under three perturbed path configurations. In each considered case, the scan path perturbations resulted in rotations and translations of defect signatures, which correlated with the detector path on approach to the respective defects. No significant signature degradation was observed that might impair detectability. The scope of this perturbation study was limited by experimental constraints that have since been removed, permitting a more extensive study to be undertaken, the results of which will be reported in due course. A predictive modelling capability was also developed and validated against experimental data. This tool will be used to inform future experimentation.

Acknowledgements

The authors would like to acknowledge Mr. Daniel Bitton, Dr. George Jung and Dr. Stephen van der Velden for their ongoing assistance in this project.

References

[1] V. Giurgiutiu, Structural Health Monitoring of Aerospace Composites, Elsevier Inc, 2016, pp. 1-23. https://doi.org/10.1016/B978-0-12-409605-9.00001-5

[2] V. Giurgiutiu, V, Structural health monitoring (SHM) of aerospace composites, in: Woodhead Publishing Series in Composites Science and Engineering - Polymer Composites in the Aerospace

Industry, second ed., Woodhead Publishing, 2020, pp. 491-558. https://doi.org/10.1016/B978-0-08-102679-3.00017-4

[3] J. Morton, E.W. Godwin, Impact response of tough carbon fibre composites, Composite Structures. 13(1) (1989) 1-19. https://doi.org/10.1016/0263-8223(89)90069-X

[4] L. Connollya, D. O'Gormana, E. Tobin, Design and Development of a low-cost Inspection UAS prototype for Visual Inspection of Aircraft, Transportation Research Procedia. 59 (2021) 85–94. https://doi.org/10.1016/j.trpro.2021.11.100

[5] S. Gholizadeh, A review of non-destructive testing methods of composite materials, XV Portuguese Conference on Fracture, Procedia Structural Integrity. 1 (2016) 050–057. https://doi.org/10.1016/j.prostr.2016.02.008

[6] S. Deane, N.P. Avdelidis, C. Ibarra-Castanedo, H. Zhang, H.Y. Nezhad, A.A. Williamson, T. Mackley, M.J. Davis, M. Maldague, A. Tsourdos, Application of NDT thermographic imaging of aerospace structures, Infrared Physics and Technology. 97 (2019), 456-466. https://doi.org/10.1016/j.infrared.2019.02.002

[7] L.E. Mavromatidis, J.L. Dauvergne, R. Lunazzi, J.C. Batsale, First experiments for the diagnosis and thermophysical sampling using pulsed IR thermography from unmanned aerial vehicle (UAV), Quantitative InfraRed Thermography. (2014) 1-8. https://doi.org/10.21611/qirt.2014.213

[8] V. Kostopoulos, S. Psarras, T. Loutas, G. Sotiriadis, I. Gray, M.J Padiyar, I. Petrunin, J. Raposo, L.Z. Fragonara, V. Tzitzilonis, K. Dassios, D. Exarchos, G. Andrikopoulos, G. Nikolakopoulos, Autonomous Inspection and Repair of Aircraft Composite Structures, IFAC-Papers OnLine. 51(30) (2018) 554-557. https://doi.org/10.1016/j.ifacol.2018.11.267

[9] M. Alhammad, N. P. Avdelidis, S. Deane, C. Ibarra-Castanedo, S. Pant, P. Nooralishahi, M. Ahmadi, M. Genest, A. Zolotas, L. Zanotti-Fragonara, J. Valdes, X. P. V. Maldague, Diagnosis of composite materials in aircraft applications: towards a UAV active thermography inspection approach, Proc. SPIE 11743, Thermosense: Thermal Infrared Applications XLIII. 1174306 (2021). https://doi.org/10.1117/12.2586064

[10] A. Ellenberg, A. Kontsos, F. Moon, I. Bartoli, Bridge deck delamination identification from unmanned aerial vehicle infrared imagery, Automation in Construction. 72 (2016) 155-165. https://doi.org/10.1016/j.autcon.2016.08.024

[11] K. Cramer, D.F. Perey, J.L. Brown, The application of line scan thermography using multiple collaborative robots, Review of Progress in Quantitative Nondestructive Evaluation. (2019).

[12] M. Lison, P. Hendrick, P. Servais, Y. Dufour, Evaluation of NDT by robotic line scan thermography on composite air-craft parts, Proceedings of the 11th International Workshop on Structural Health Monitoring, IWSHM 2017. 1 (2017) 86-93. https://doi.org/10.12783/shm2017/13853

[13] F. Khodayar, F. Lopez, C. Ibarra-Castanedo, X. and Maldague, Optimization of the Inspection of Large Composite Materials Using Robotized Line Scan Thermography, Journal of Nondestructive Evaluation. 36 (2017), 1-15. https://doi.org/10.1007/s10921-017-0412-x

[14] S. Deane, N. P. Avdelidis, C. Ibarra-Castanedo, A.A Williamson, S. Withers, A. Zolotas, X. Maldague, M. Ahmadi, S. Pant, M. Genest, H.A. Rabearivelo, A. Tsourdos, Development of a thermal excitation source used in an active thermographic UAV platform, Quantitative InfraRed Thermography Journal. (2022) 1-32. https://doi.org/10.1080/17686733.2022.2056987

[15] J. Moran, N. Rajic, Remote line scan thermography for the rapid inspection of composite impact damage, Composite Structures. 208 (2019) 442-453. https://doi.org/10.1016/j.compstruct.2018.10.038

[16] J. Gray, M. Woodrow, C. Rosalie, N. Rajic, Comparative evaluation of a high operating temperature midwave infrared detector for automated non-destructive inspection of composite damage, Materials Research Proceedings, 8APWSHM. 18 (2020) 29-36.

[17] J. Gray, P. Muir, J. Denny, C. Rosalie, H. Self, N. Rajic, Rapid non-destructive inspection of composite laminates using robotic line-scan thermography. AIAC 2021: 19th Australian International Aerospace Congress. 1 (2021) 393-399.

[18] X. Maldague, S. Marinetti, Pulse phase infrared thermography, Applied Physics. 79 (1996) 2694-2698. https://doi.org/10.1063/1.362662

[19] K. Lynch, F. Park, F, Modern Robotics: Mechanics, Planning and Control, Cambridge University Press, 2017, Ch. 13, pp 513-527.

[20] M. Crenganis, C. Biris, C. Girjob, Mechatronic Design of a Four-Wheel drive mobile robot and differential steering, MATEC Web Conference. 343 (2021). https://doi.org/10.1051/matecconf/202134308003